Article

FAP-Targeted Fluorescent Imaging Agents to Study Cancer-Associated Fibroblasts In Vivo

Riley J. Deutsch-Williams, Kelton A. Schleyer, Riddha Das, Jasmine E. Carrothers, Rainer H. Kohler, Claudio Vinegoni, and Ralph Weissleder*

Cite This: https://doi.org/10.1021/acs.bioconjchem.4c00426
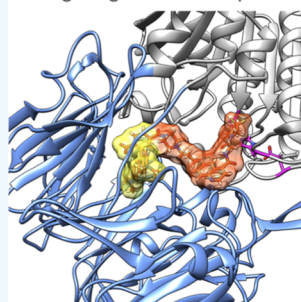
Read Online

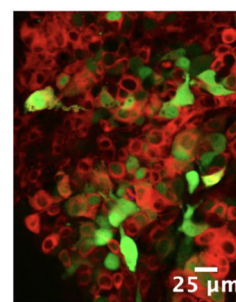| ACCESS | Metrics & More | Article Recommendations | Supporting Information |

ABSTRACT: Cancer-associated fibroblasts (CAFs) expressing fibroblast activation protein alpha (FAP) are abundant in tumor microenvironments and represent an emerging target for PET cancer imaging. While different quinolone-based small molecule agents have been developed for whole-body imaging, there is a scarcity of well-validated fluorescent small molecule imaging agents to better study these cells in vivo. Here, we report the synthesis and characterization of a series of fluorescent FAP imaging agents based on the common quinolone azide inhibitor. Our data show excellent performance of some synthesized FAP Targeting Fluorescent probes (FTFs) for both topical application and intravenous delivery to label CAF populations in solid tumors. These results suggest that FTF can be used to study CAF biology and therapeutic targeting in vivo.

Synthesis and validation of FAP targeting fluorescent probes

In Vivo Analysis of FAP+ cells

25 μm

INTRODUCTION

Cancer-associated fibroblasts (CAFs) are a major population of stromal cells within or adjacent to tumor tissue that have gained much interest as a diagnostic and therapeutic target. CAFs play myriad roles in tumorigenesis, including remodeling of the extracellular matrix to promote cancer invasion, tumor metabolic alterations via metabolite shuttling, and interference with immune cell function.[1] CAFs make up a considerable cellular portion of epithelial cancers. Some studies have estimated that tumor stroma may contribute to as much as 60−90% of the total tumor mass,[2,3] while others have estimated fibroblasts compose one-third of all stromal cells in a tumor.[4] Given their abundance, CAFs have been proposed as a pancancer marker. Single-cell RNaseq studies have elucidated many subtypes ranging from 4 to 10 across different studies.[5,6] Across this heterogeneity, certain markers are widely observed, including fibroblast activation protein alpha (FAP; DPPIV) and smooth muscle actin, which have been used in previous studies to define CAFs before sequencing. FAP-positive CAFs generally include the mCAF, iCAF, tCAF, hsp_tCAF, ifnCAF, apCAF, dCAF, and dCAF subtypes.[5] FAP is a secreted protein that has di- and endoprolylpeptidase, endoprotease, and gelatinase/collagenase activities in the tumor microenvironment. The presence of FAP-positive CAF subtypes has been observed across many cancer types and has been linked to poor clinical outcomes. For example, in colorectal cancer, FAP contributes to adverse clinical outcomes such as increased lymph node metastasis, tumor recurrence,

and angiogenesis, as well as decreased overall survival.[7] In breast cancer, FAP-expressing CAFs are associated with an increased risk of recurrence[8] and have been shown to promote an immunosuppressive environment.[9]

FAP is an alluring tumor target owing to low expression in normal fibroblasts and healthy tissues and much higher expression in activated fibroblasts.[10] A number of different imaging agents have been developed for FAP PET imaging, including antibodies,[11] peptides,[12] and small molecule compounds.[13] Most FAP inhibitor (FAPi) PET agents belong to a quinoline-based class of small molecule inhibitors.[13−15] Despite the abundance of PET imaging agents,[16,17] fluorescent companion imaging agents have generally not been developed or employed to study fibroblasts in vivo at the single cell level.

Here, we synthesized and systematically validated a number of different fluorescent quinoline derivatives,[14] obtained through intermediates to ensure performance at single-cell resolutions. We began by characterizing the functional and imaging performance of these fluorescent analogues to ensure proper biological behavior. Inhibition assays demonstrate that each of the synthesized agents had nanomolar binding affinity
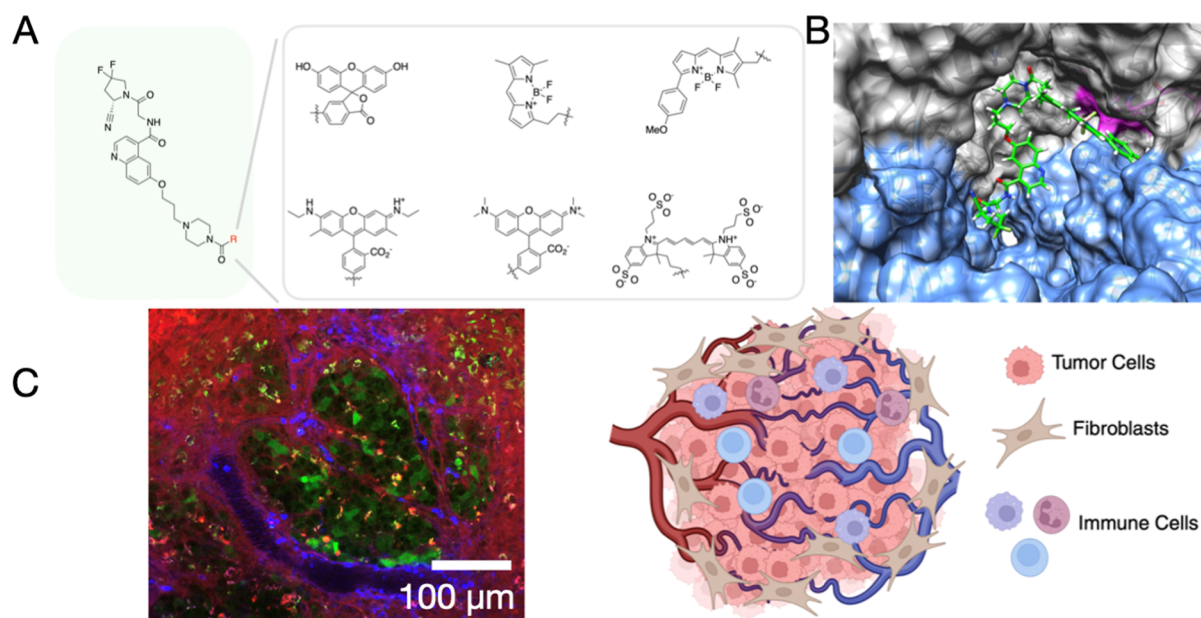
Figure 1. Overview of FTF synthesis, validation, and utilization. (A) Six different FTF imaging agents were synthesized by conjugating fluorophores to a FAP-binding precursor (green) via an aminopiperazine linker. (B) FTF agents were validated chemically using a variety of in silico and in vitro techniques. (C) Validated FTF agents were leveraged in vivo to explore compound delivery and distribution and to characterize single-cell uptake.

to FAP. Further, we demonstrate the colocalization of the FAP-targeted fluorescent probes (FTF) with immunohistochemical staining for FAP. The validated FTF probes were then used in vivo tumor models to characterize the cellular and intratumoral spatial distribution of FAP signal. To our knowledge, this work demonstrates the first microscopic analysis of FAP-based cellular imaging in an intravital tumor model.

RESULTS

Synthesis and Characterization of FTF Conjugates. To synthesize a small collection of FTF conjugates (Table S1, Figure 1), we used the commercially available FAP-IN-2 precursor, an azide quinolone derivative that binds to the canonical FAP catalytic binding site consisting of the triad Ser624, His734, and Asp702. This structure was conjugated to six different NHS-activated fluorophores(BODIPY dyes, Fluorescein, Rhodamines, Alexa Fluor). Figure 2 outlines the single-step reaction used for synthesis of each compound, and the final structures with their respective masses are reported in Figure S1. Yields ranged from as low as 21.4% (Fluorescein-FAPi) to 85.6% (BODIPY FL-FAPi). Following purification with reverse-phase high performance liquid chromatography (HPLC) compounds were >98% pure and used for further characterization (Table S1).

The successful generation of each purified product was determined using Liquid chromatography−mass Spectrometry (LC−MS) (LCMS). Mass traces for each compound can be found in Figure S2. As shown, each compound eluted in a single peak with retention times as follows: FTF-Fluorescein −2.53 min; FTF-BODIPY = FL—5.51 min; FTF-BODIPY-TMR—4.69 min; FTF-Rhodamine6G—2.72 min; FTF-TAMRA—3.64 min; FTF-AF647−4.14 min. We also performed Nuclear Magnetic Resonance (NMR) spectroscopy to confirm the expected structures: the ^{1}H NMR aromatic region (δ 6.5−9.5 ppm) of FTF-BODIPY-TMR (Figure S3)

and FTF-TAMRA (Figure S4) contained signature peaks for the quinoline moiety of FAP-IN-2 and for the respective fluorophores, consistent with successful conjugation. Conjugation of fluorophores to FAP-IN-2 did not impact the fluorescent properties of the dye molecules. Absorption and emission spectra were collected on a plate reader and are presented in Figure S5.

We next assessed the IC_{50} of each FTF conjugate using the fluorogenic FAP substrate, Z-Gly-Pro-AMC, and recombinant murine FAP. As shown in Figure 3, each FTF conjugate displayed a single-digit nanomolar IC_{50} value (Fluorescein = 0.157 nM; BODIPY-FL = 2.62 nM; BODIPY-TMR = 7.84 nM; Rhodamine6G = 7.60 nM; TAMRA = 1.07 nM; AF647 = 1.04 nM). This places the inhibitory effect of each FTF conjugate, within 1 order of magnitude of FAPi-4 (IC_{50} = 0.59 nM, Figure S6). This suggests that fluorophore conjugation does not inhibit the FAP pocket binding capabilities of the quinoline structure. Variation between IC_{50} values for our FTF conjugates can be attributed to varying levels of steric hindrance and hydrophobicity by the dye when in the FAP binding pocket. To further explore how various FTF conjugates interact with FAP, we performed molecular modeling to further assess the arrangement of the FTF conjugates in FAP. Figure S7 shows the modeling for FTF-BODIPY TMR whereas Figure S8 shows the modeling for FTF-TAMRA. Both models show that the fluorophore does not alter the quinolone binding to the active site pocket. We also determined whether other FAP affinity ligands, such as the FAPi-46 precursor, would be a preferable scaffold. We found similar docking scores (of 8.188 and 8.268 for FAP-IN4 and FAPi-46 with TAMRA), indicating similar binding poses-(Figure S9).

Co-Localization of FTF Compounds with FAP Antibody Staining. To perform colocalization experiments between the different small molecule companion imaging agents and a FAP-labeled antibody, we used one of the few
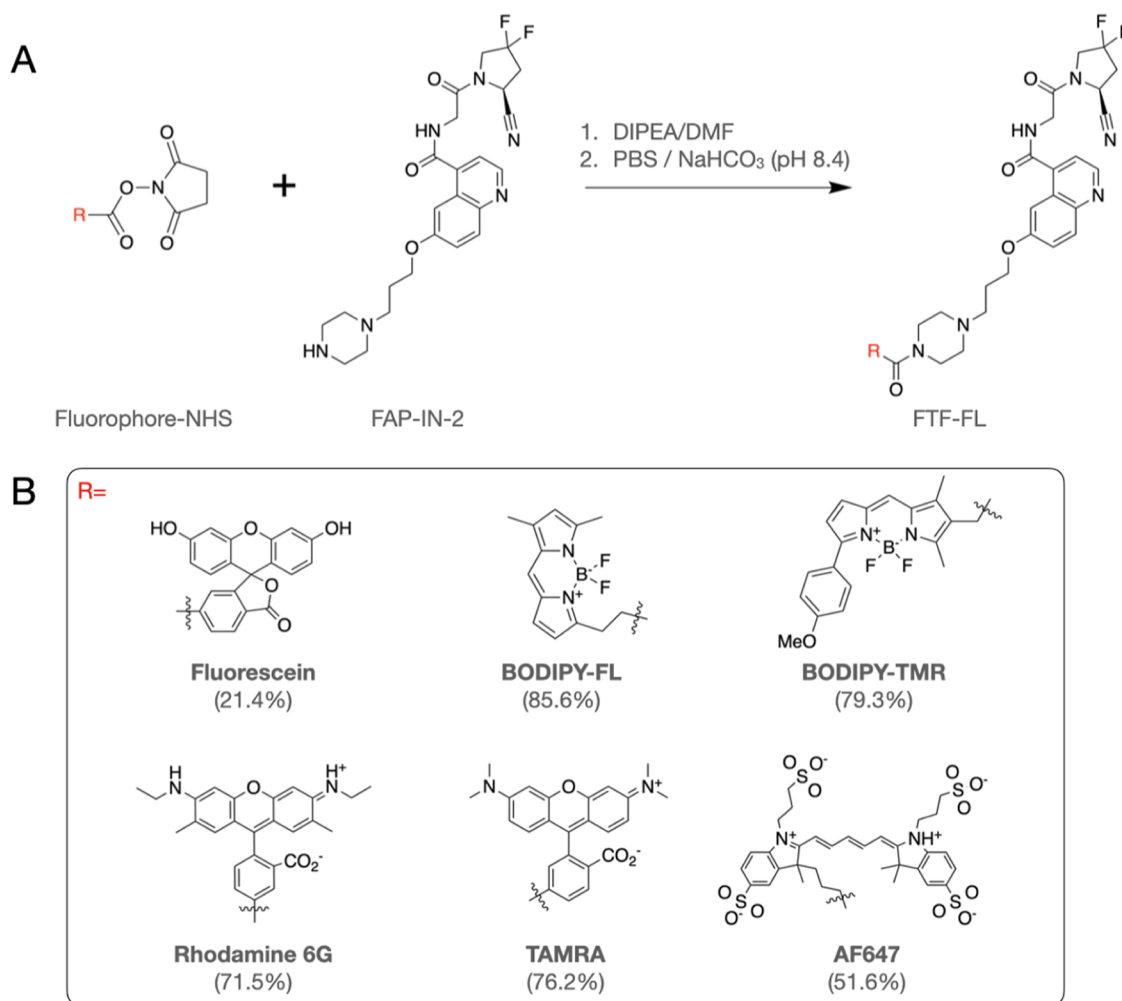
Figure 2. Synthesis of FTF imaging agents. Six different NHS ester activated fluorophores were reacted with FAP-IN-2 precursor, in a single-step synthesis. Yields for various conjugates ranged between 20 and 80% depending on reaction. The lead compounds, FTF-TAMRA and FTF-BODIPY-TMR, were synthesized at ~80% yield. Compounds were purified via HPLC and lyophilized to yield a dry powder and resuspended in stocks of dimethyl sulfoxide (DMSO) to be further diluted for subsequent use.

FAP-expressing tumor cell lines (U138-MG). Cells were first stained with 500 nM of FTF followed by a wash, fixation, and staining with an anti-FAP antibody. Figure 4A contains representative images of stained cells. Visually, distinct regions of high FTF/low antibody signal can be observed in the merged FTF-AF647 at the edges of the cell. To quantify colocalization of the two signals, binned scatter plots were created (Figure 4B) with antibody signal on the X axis and FTF signal on the Y axis. For each distribution, a Pearson's Correlation coefficient was calculated (Fluorescein = 0.66; BODIPY-FL = 0.89; BODIPY-TMR = 0.82; Rhodamine6G = 0.83; TAMRA = 0.92; AF647 = 0.46). This points to strong colocalization between FTF accumulation and antibody binding in all conjugates except for FTF-Fluorescein and FTF-AF647. Further, the slopes of the distributions for FTF-BODIPY-FL and FTF-Rhodamine6G are shallower than for FTF-TAMRA and FTF-BODIPY-TMR. This suggests a narrower dynamic range for these probes and led us to move forward with FTF-BODIPY-TMR and FTF-TAMRA as our lead candidates.

Imaging the Tumor Microenvironment Confirms Probe Specificity. We next performed a series of experiments to determine the distribution of one of the two lead imaging compounds, FTF-BODIPY-TMR. In the first set of experiments, we determined the cellular location of FTF-BODPIY-TMR staining in the B16 F10 TagGFP tumor model of excised tumors (Figure 5). As seen in Figure 5A, FTF-BODIPY-TMR signal accumulates within specific cells of the tumors. When looking at the signal in the tumor compared to the signal in the surrounding tissue, FTF displays a higher signal-to-background (3.3 in FTF compared to 1.6 in the GFP image), suggesting excellent bulk tumor-specific contrast. To determine which cells the FTF probe accumulates in, we obtained higher-resolution imaging. These data show that FTF-BODIPY-TMR predominately accumulates in nontumor cells (Figure 5B), i.e., host cells lacking the GFP-tumor markers. At higher resolutions, It was possible to visualize the spindle-like morphology of the FTF-positive cells (Figure 5C). In comparison, FTF-TAMRA also labeled individual nontumor cells (Figure S10A−B). Higher levels of diffuse fluorescence were observed compared to FTF-BODIPY-TMR (Figure S10C).

Given the superb imaging performance we next attempted to use FTF-BODIPY-TMR for in vivo use. We observed that FTF-BODIPY-TMR would not solubilize in saline beyond a concentration of 10 mg/mL. This was prohibitive to injecting
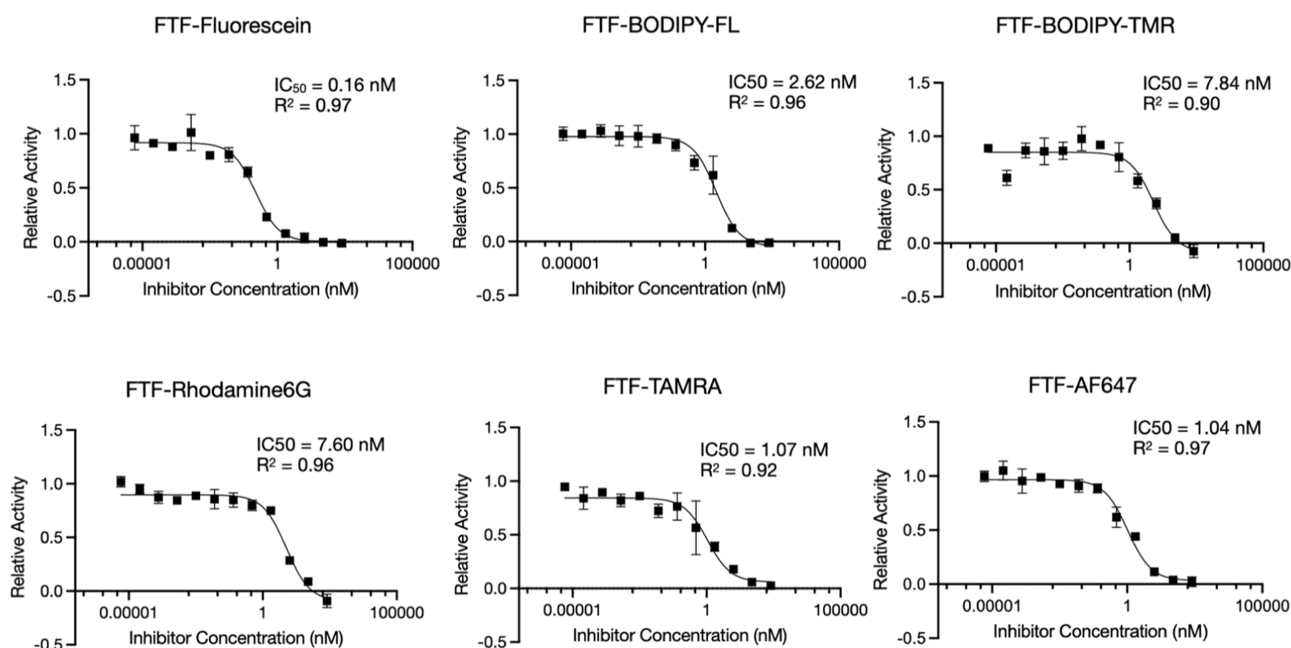
Figure 3. FAP affinity of different fluorescent imaging compounds. IC_{50} calculations each of the FTF conjugates. Recombinant murine FAP activity was measured using the fluorogenic FAP substrate Z-Gly-Pro-AMC. Concentrations of FTF spanned from 5 pM to 250 nM and are plotted on a logarithmic axis. Relative activity (*y* axis) was scaled to measurements from wells with (1) FAP and Z-Gly-Pro-AMC but no inhibitor, and (2) Z-Gly-Pro-AMC but no FAP or inhibitor. IC_{50} (expressed as nM concentration in the graphs) was determined from a nonlinear, three-parameter, inhibitor vs response curve fit.

sufficient dye intravenously in a 100 μL bolus. Further estimates of the octanol−water partition coefficients of each FTF conjugate are summarized in Table S1 and confirm the greater hydrophobicity of FTF-BODIPY-TMR to FTF-TAMRA. We thus chose FTF-TAMRA as the IV injectable imaging agent.

FTF-TAMRA had ideal imaging characteristics for in vivo use following intravenous injection. To characterize the intravenous delivery and accumulation of FTF-TAMRA, we performed intravital imaging in dorsal window chambers (DWC) and flow cytometry on flank tumors (Figure 6A). Briefly, FTF-TAMRA was injected via the tail vein, and allowed to accumulate for 60 min before final images were collected or tumors were excised for flow cytometry. Blood half-life was fit from intravital images collected over an hour to a biphasic exponential decay ($R^2 = 0.99$) and with a fast half-life of 1.9 min and a slow half-life of 10.1 min(Figures 6B and S11). The FTF imaging probe subsequently accumulated in target cells over time with signal intensities peaking shortly after vascular clearance (around 40 min), and beginning to clear at 2 h postinjection. The tissue signal returned to baseline levels 24 h later. Based on these kinetics, we performed flow cytometry on excised B16 F10 tumors following FTF-TAMRA injections. We observed that nearly 80% of the FTF signal accumulated in stromal cells, 20% accumulated in immune cells, and less than 0.1% of FTF-labeled cells were tumor cells (Figure 6B). Further analysis revealed that of the FTF + immune cell population, the large majority (67%) of cells were macrophages. Similarly, we found that 47% of the stromal cells analyzed were double positive for podoplanin and α-SMA, suggestive of a myo-CAF subtype (Figure S12). Our intravital imaging further corroborated these findings. We observed regions of high FTF signal where there were few tumor cells (Figure 6C), which at higher magnifications appeared to be dense regions of fibrotic tissue (Figure 6D). We also observed

regions of FTF-labeled cells interspersed with tumor cells (Figure 6E,F). In each of these cases, we observed no colocalization of FTF signal and GFP-labeled tumor cells.

◼ DISCUSSION

We have synthesized and validated a series of FAP fluorescent imaging agents by conjugating fluorophores to a FAP affinity ligand featuring an azide for protein cross-linking with nanomolar affinity. We show that the synthesized fluorescent compounds retain nanomolar FAP affinity in competitive inhibition assays. Interestingly, the agents showed different biological behaviors with one clearly preferred agent emerging. This compound (FTF-TAMRA) had a molecular weight of 867 g/mol, was able to be synthesized at ∼80% yield, and achieved a close correlation when compared to anti-FAP antibody staining of semipermeabilized cells. Compared to antibody labeling methods, our FTF probes offer the advantage of more rapid delivery. A smaller size and moderate hydrophobicity of the quinoline azide also allows for cell permeability and in vivo utility. To date, only a few studies have described fluorescent FAP companion imaging agents, but mostly for macroscopic imaging to characterize bulk tumor uptake[18,19] or to observe ex vivo contrast in FAP-over-expressing transfected xenograft models.[20] Our lead compounds differ from the described agents in that (1) they were validated and employed for single cell imaging of in vivo tumors (2) they were synthesized in a single step reaction, using readily available starting materials, outlining a straightforward protocol for others to begin imaging with fluorescent FAP analogs without the need for complicated synthesis.

FAP-In-2 was chosen as the molecular scaffold as considerable work has been done in the past[15] and because it is a commercially available intermediate widely available to the research community. Importantly, previous work with
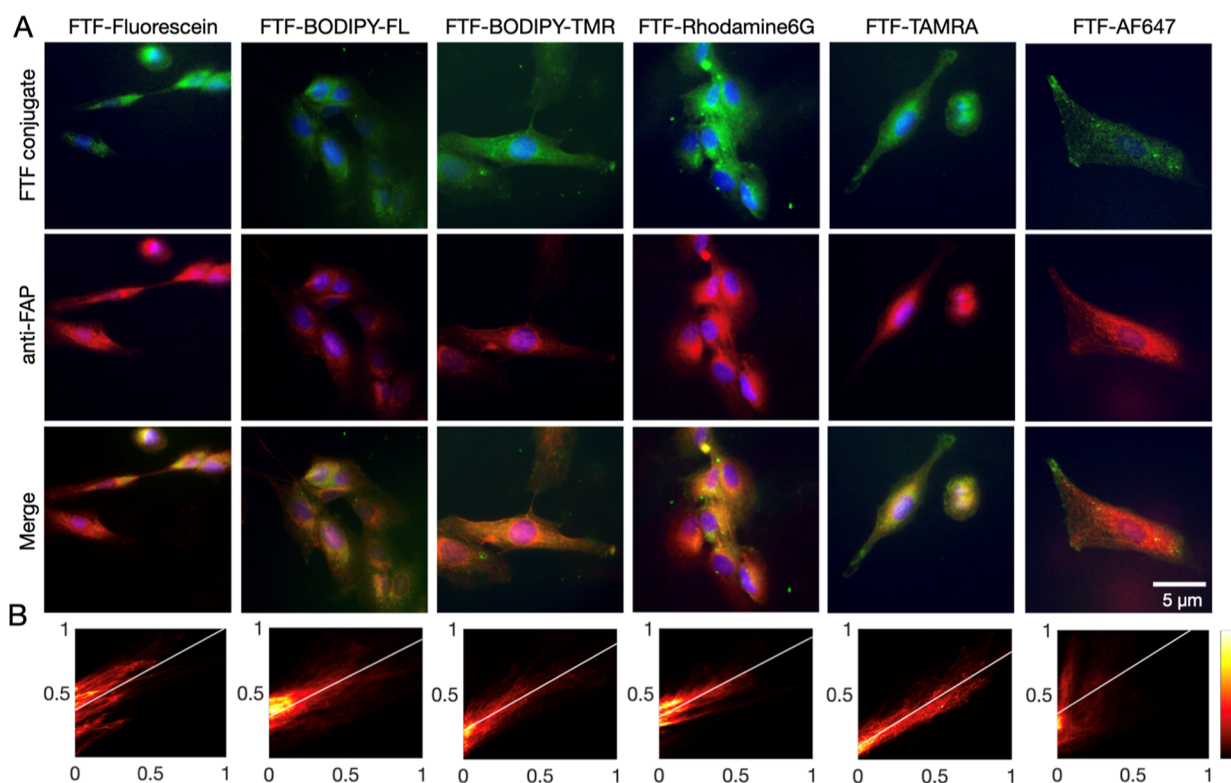
Figure 4. Co-localization of synthesized FTF conjugates with anti-FAP immunocytochemistry. Cell imaging experiments were conducted in the FAP-expressing U138-MG cell line. (A) Representative fluorescent images of cells stained with 500 nM of each of the FTF conjugates and an anti-FAP antibody. Row one displays FTF fluorescence (false color green); row two displays anti-FAP fluorescence (false color red) generated by secondary antibody staining labeled with either AF488 or AF647; Row three displays a merge of the two signals. All images include a DAPI nuclear stain in blue. Imaging was performed in triplicate for each condition, and representative images magnified subregions of single images to highlight intracellular features. (B) Binned scatter plots depicting the colocalization of FTF conjugate (y-axis) and anti-FAP antibody (x-axis) signal. Scatter plots represent cumulative pixel data from three sets of images for each condition. A linear regression was performed for each data set and the resulting best-fit line is plotted in white. A narrower spread of pixels about this line indicates a better correlation (e.g., see TAMRA and BODIPY-TMR). Pearson's correlation coefficient was calculated for each scatter plot.

quinolone azide-based FAP inhibitors has established the specificity of the scaffold to FAP. For instance, the scaffold used in our work has a >1000x affinity for FAP compared to other proteins in the same family of serine proteases including DPPII, DPP IV, DPP 9, and PREP.[14] More recently, subtle changes in the structure have led to FAPi-46 compounds often used for nuclear imaging. Our molecular modeling showed that these two compounds have similar binding affinities for the catalytic site of the FAP binding pocket. Further, our imaging experiments demonstrate clear labeling of cancer associated-stromal cells, with negligible off-target binding to tumor cells. We observed excellent fibroblast accumulation of FTF-TAMRA in vivo with kinetics conductible to imaging. For example, we observed that fibroblast accumulation occurred as soon as 30 min postinjection, and began to clear after 2 h. These kinetics were considerably faster than anti-FAP antibody imaging. Using different mouse models, we estimate that nearly 80% of FTF-FL-positive cells are stromal cells, with nearly all expressing at least a single CAF marker other than FAP. While the FTF probes were validated on murine FAP, we expect the probes would perform equally well on cells expressing human FAP owing to a shared 90% identity and 94% similarity on an amino acid level. Further, previous studies with quinoline azide-based inhibitors demonstrated affinity for both human and murine FAP.[21]

The current proof-of-principle study points to several future directions. First, given the considerable interest in the field of FAP PET imaging, new scaffolds are constantly being explored, and these could be used for fluorescence imaging, yielding agents with even higher selectivity for fibroblasts. As these reagents become commercially available, it would be straightforward to apply the described validation pipeline to new FTF optical imaging agents. Second, while we performed kinetic experiments of tumor uptake of our probes in vivo, the fluorescent companion imaging agents could be used to better understand the pharmacokinetics and dynamics of theranostic counterparts. Understanding the distribution of FAPi compounds at the cellular level may help to design novel theranostic agents. Third, while dorsal window chamber models are commonly employed to study cancer biology, specialty chamber models may be required for brain, breast, liver and gastrointestinal tumors.[22−25] Future studies targeted at these sites may help elucidate how healthy stromal cells are recruited to a FAP-expressing, tumorigenic phenotype. Fourth, investigating alternative FTF conjugates with red- or NIR-emitting fluorophores that exhibit comparable FAP binding to FTF-BODIPY-TMR and FTF-TAMRA could enable deeper tissue imaging for intraoperative applications. Finally, while we focused on "always-on" FAP agents in this study, it is conceivable to develop "off-agents"[26] or bioorthogonal click imaging agents for in vivo use.[27] Irrespective of these caveats,
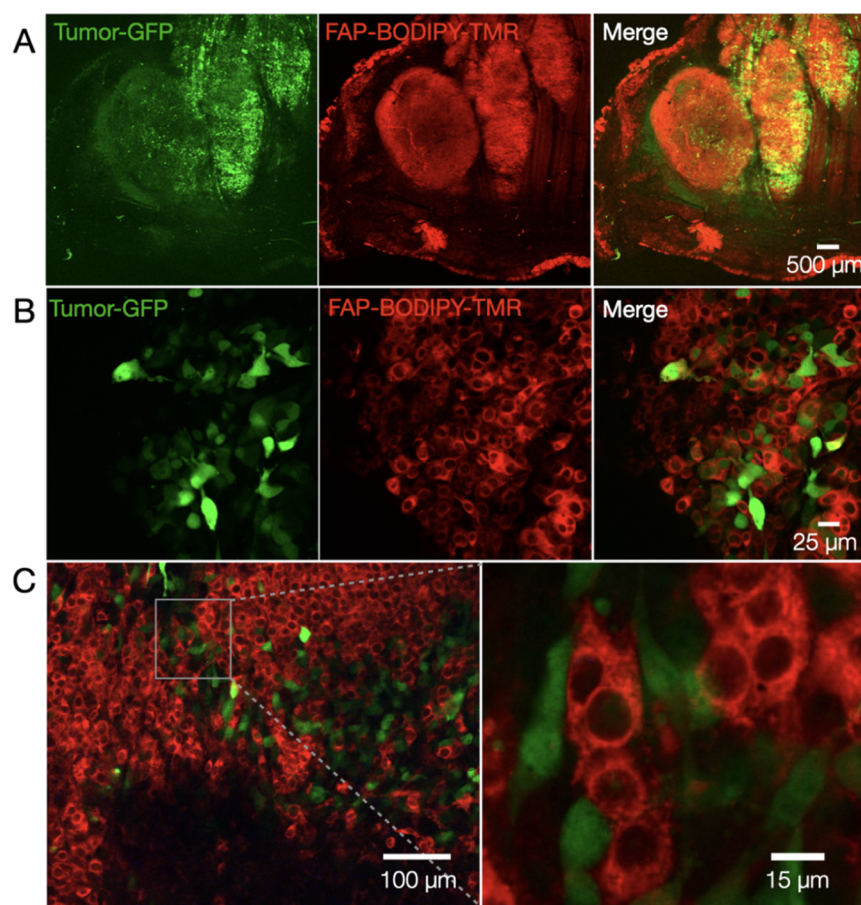
Figure 5. Cellular distribution of FTF in ex vivo murine tumors. (A) Low-resolution images of ex vivo B16 F10 GFP tumors grown in the flank of C57BL/6 mice ($n = 3$). Tumors were stained topically in a solution of 1 μM of FTF-BODIPY TMR and 5 μg/mL Hoechst (blue) for 10 min. The merged image of the three channels reveals macroscopic coincidence between FTF signal, tumor GFP, and nuclear density (Hoechst). (B) Single-cell resolution in vivo imaging of FTF stained B16 F10 GFP tumors. (C) High-resolution imaging shows the FTF-positive cells to be largely spindle-shaped and devoid of tumor cells GFP.

our data clearly show the utility of the developed imaging agents.

■ MATERIALS AND METHODS

Materials. All reagents and solvents were procured from Thermo Fisher or Sigma-Aldrich employed without further purification. Fibroblast activation protein inhibitors FAP-In-2 TFA (purity: 99.92%) and FAPi-4 were procured from MedChemExpress. The NHS esters of BODIPY TMR, BODIPY FL, Rhodamine6G, TAMRA, and Fluorescein were purchased from Lumiprobe. The NHS ester of Alexa Fluor 647 was purchased from Thermo Fisher. All starting materials were reconstituted in dry DMSO and utilized without further processing.

Synthesis of FTF. *N,N*-Diisopropylethylamine (DIPEA) (14 μL, 80 μmol) was added to a solution of fluorophore succinimidyl ester (30 μL, 84 μmol) and FAP-IN-2 (20 μL, 84 μmol) in DMSO (100 μL). Sodium bicarbonate in PBS (50 μL, 0.1 μM; pH 8.4) was added and the reaction mixture was stirred for 16 h at room temperature. Product was purified via HPLC (0−100% acetonitrile/H_2O with 0.1% formic acid) to yield >98% pure FLT conjugates which were lyophilized for storage.

FTF-TAMRA. ^{1}H NMR (400 MHz, DMSO): δ 9.11 (d, J = 6.5 Hz, 1H), 8.83 (d, J = 4.4 Hz, 1H), 8.17 (d, J = 7.9 Hz, 1H), 8.06 (d, J = 7.9 Hz, 1H), 7.98 (t, J = 9.2 Hz, 2H), 7.88 (s, 1H), 7.70 (d, J = 7.9 Hz, 1H), 7.57−7.50 (m, 2H), 7.46 (dd, J = 9.2, 2.4 Hz, 1H), 7.22 (s, 1H), 5.15 (d, J = 9.6 Hz, 1H), 4.34 (t, J = 13.0 Hz, 1H), 4.25 (d, J = 6.0 Hz, 1H), 4.16 (d, J = 21.8 Hz, 2H), 3.59 (s, 1H), 3.21 (s, 1H), 2.83 (t, J = 17.8 Hz, 2H), 2.32 (s, 2H), 1.96 (s, 2H).

ESI-MS for FTF-TAMRA. m/z: calcd 897.97; found, 897.8.

FTF-BODIPY-TMR. 1H NMR (400 MHz, DMSO): δ 9.10 (t, J = 6.1 Hz, 1H), 8.80 (d, J = 4.3 Hz, 1H), 8.24 (s, 2H), 7.97 (d, J = 9.2 Hz, 1H), 7.89−7.82 (m, 3H), 7.69 (s, 1H), 7.51 (d, J = 4.4 Hz, 1H), 7.43 (dd, J = 9.2, 2.7 Hz, 1H), 7.14 (d, J = 4.1 Hz, 1H), 7.04−6.97 (m, 2H), 6.69 (d, J = 4.1 Hz, 1H), 5.12 (dd, J = 9.3, 2.9 Hz, 1H), 4.39−4.28 (m, 1H), 4.27−4.20 (m, 2H), 4.13 (t, J = 6.6 Hz, 2H), 3.81 (s, 3H), 3.50 (s, 1H), 3.40 (d, J = 23.7 Hz, 4H), 2.87 (dd, J = 28.2, 13.3 Hz, 2H), 2.62 (t, J = 7.6 Hz, 2H), 2.54 (s, 1H), 2.44 (d, J = 12.6 Hz, 7H), 2.29 (dd, J = 12.2, 7.5 Hz, 3H), 2.22 (s, 3H), 1.92 (t, J = 7.0 Hz, 2H), 1.23 (s, 2H), 0.93−0.74 (m, 2H).

ESI-MS for FTF-BODIPY-TMR. m/z: calcd 865.73; found, 865.8.

Characterization. *Nuclear Magnetic Resonance (NMR).* NMR spectra were recorded on a Bruker Avance UltraShield 400 MHz spectrometer. 1H NMR chemical shifts are reported in ppm relative to SiMe4 (δ = 0) and were referenced internally with respect to residual protons (δ = 2.50 for DMSOd6 and δ = 4.79 for D2O). Coupling constants are reported in Hz. Peak assignments are based on calculated
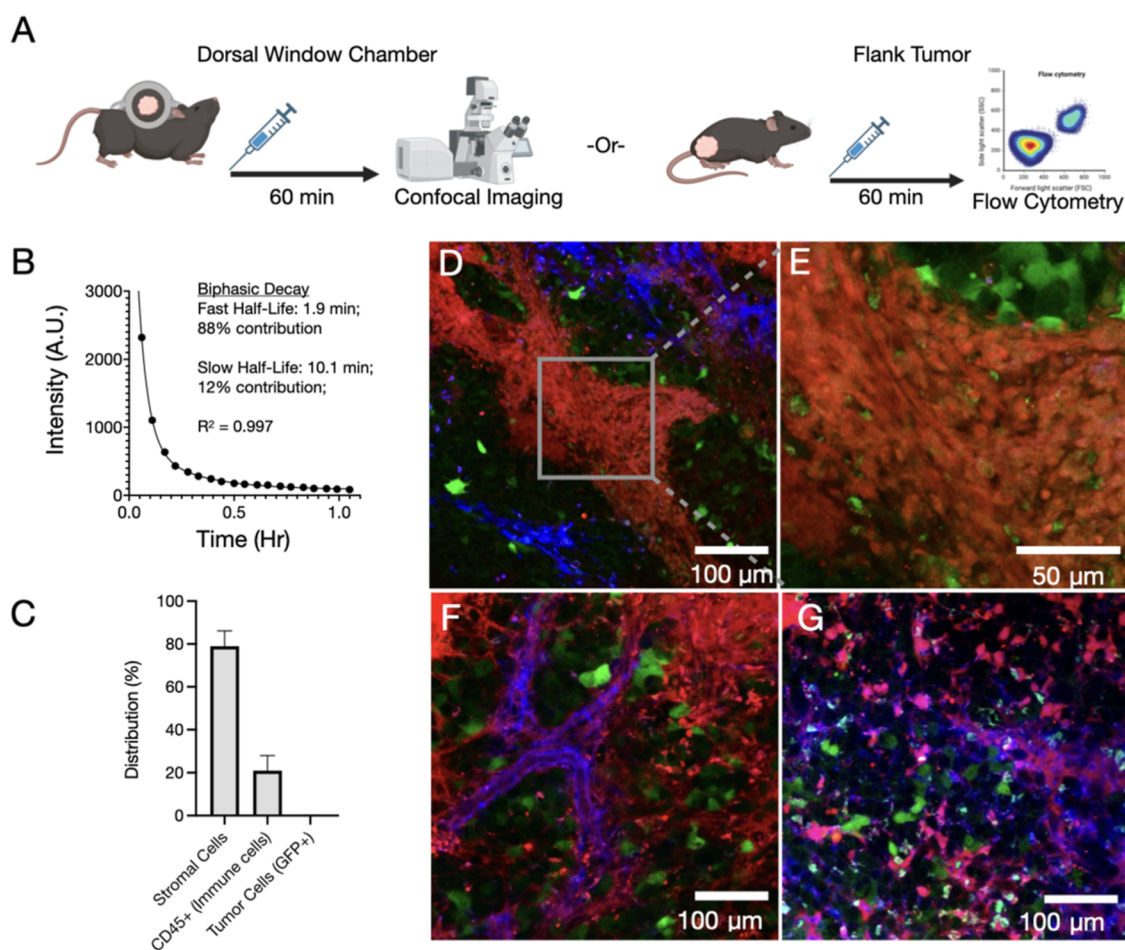
Figure 6. Intravenous delivery of FTF to B16 tumor model. (A) Schematic of in vivo imaging experiments performed (B) Blood Half-life measurement of FTF-TAMRA delivered systemically via tail vein injection in B16 tumor-bearing mice (100 μg of FTF-TAMRA in 100 μL of saline was injected via the tail vein). (C) Flow cytometry results determining subtypes of FTF stained cells. (D) Intravital image of FTF-TAMRA (red) accumulation in fibrous regions of B16 F10 GFP (green) tumors. Vasculature is labeled with TD-lectin-Dylight647 (blue). (E) Higher resolution image illustrates density FTF stained cells. (E) Intravital image if FTF distribution near a vessel. (F) FTF-stained cells interspersed with tumor cells.

chemical shifts, multiplicity and 2D experiments. IUPAC names of all compounds are provided and were determined using CS ChemBioDrawUltra 15. NMR spectra processing and analysis was performed with MesReNova Research S.L (version 15.0.1). In some cases, Multipoint Baseline Correction was used to smooth rolling baselines; all genuine signals were retained during this process.

Liquid Chromatography–Mass Spectrometry (LC–MS). High performance LC–MS analysis was performed on a Waters instrument equipped with a Waters 2424 ELS Detector, Waters 2998 UV–Vis Diode array Detector, Waters 2475 Multiwavelength Fluorescence Detector, and a Waters 3100 Mass Detector. Separations employed an HPLC-grade water/acetonitrile solvent gradient with an XTerra MS C18 Column, 125 Å, 5 μm, 4.6 mm × 50 mm column; Routine analysis were conducted with 0.1% formic acid added to both solvents.

Optical Spectra. FTF analogues were diluted to a concentration of 1 μM in either DMSO (BODIPY FL, BODIPY TMR) or PBS (Fluorescein, Rhodamine6G, TAMRA) Absorbance and fluorescence spectra were performed with a multimode microplate reader (Tecan, Spark 500) using 96-well transparent bottom black polystyrene microplates (Corning). Absorption was measured from 400 to

700 nm in 1 nm steps for all compounds. Excitation and emission settings for fluorescence spectra measurements were tailored to each conjugate and are summarized in Table S2. All spectra were measured in triplicate, and the background was corrected from measurements of blank wells. Spectra were smoothed using a moving average filter with a smoothing factor of 0.01 and a window size of 5. All calculations were done in MATLAB 2023B (Mathworks, Natick, MA).

Inhibition Assay. The inhibitory effect of FTF compounds was measured using the fluorogenic FAP substrate, Z-Gly-Pro-AMC (MedChemExpress). Briefly, recombinant mouse FAP (BioLegend) was diluted to a concentration of 0.01 μg/100 μL. Serially diluted (1:5) aliquots of FTF spanning concentrations from 10 pM to 10 μM were added to the protein solution and incubated for 30 min at 37 °C. After this initial incubation, 10 μL of a 100 μM solution of Z-Gly-Pro-AMC were added to each well and incubated for 60 min at 37 °C. Z-Gly-Pro-AMC fluorescence was measured with a multimode microplate reader (Tecan, Spark 500) using 96-well transparent bottom black polystyrene microplates (Corning) (E_x = 380, E_m = 460). All dilutions were performed with an assay buffer consisting of 50 mM Tris, 1.0 M NaCL, and 0.1% BSA (w/v) at a pH of 7.5.

Docking Studies. Docking simulations were performed using the Schrödinger computational software (Release 2024-3; Glide, Schrödinger LLC, New York, NY) The structure of FAP was obtained from the RCSB database (PDB ID: 1Z68). We prepared the structure for docking by performing energy minimization, optimizing the hydrogen bonding interactions, and removing extraneous waters and molecules. We then prepared our ligands using the OPLS4 force field and created three docking grids within the binding pocket of FAP that correspond with the catalytic triad, S1′, and S2′ subpockets of the binding site. Molecular graphics images were produced using the Chimera package from the Computer Graphics Laboratory, University of California, San Francisco (supported by NIH P41 RR-01081).

Cell Culture. Cells were plated and cultured in Dulbecco's Modified Eagle Medium (DMEM, Corning) supplemented with 10% Fetal Bovine Serum (Corning) and 1% penicillin Streptomycin (Corning) at 37 °C and 5% CO_2. Cells were passaged with 0.05% trypsin−EDTA (Corning). For in vitro imaging studies, U138-MG human glioblastoma (ATCC) cells were used as a FAP positive cell line (https://www.proteinatlas.org/ENSG00000078098-FAP/cell+line) and NIH-3T3 murine fibroblast cells were used as a FAP negative cell line. For all in vivo imaging, B16 F10 (ATCC) murine melanoma cells were transfected with GFP as previously described[28] and utilized for all in vivo imaging.

Widefield In Vitro Microscopy. Forty-8 h prior to the start of the experiment, 5000 U138-MG cells were seeded on a Millicell EZ Slide (Millipore Sigma). Twenty-4 h prior to imaging, cells were stained with 500 nM of FAPi-FL conjugate for 1 h in serum free media. Cells were rinsed for 40 min in 40 h in serum free media follow by a rinse in PBS and a 10 min fixation with 4% paraformaldehyde—PBS (PFA, Corning). Subsequently, cells were washed with PBS for 2 min followed by permeabilization with 0.5% Triton X-100 (Thermo Fisher) in PBS for 5 min and a 5 min wash with PBS. Fixed cells were then blocked in Intercept Blocking Buffer (LI-COR) for 1 h. After blocking, cells were stained with 5 μg/mL solution of anti-FAP antibody (Thermo Fisher, polyclonal: PA5-120990) for 16 h. After three 2 min washes with PBS, cells were stained with the appropriate antirabbit secondary antibody (Thermo Fisher) for 1 h. After washing, cells were stained with 1 μg/mL DAPI for 5 min. An Olympus BX-63 upright automated epifluorescence microscope was used to acquire fluorescent images. DAPI, FITC, Cy3, and Cy5 filter cubes were used to excite the appropriate fluorophore in each sample.

Flow Cytometry. C57BL/6J mice bearing B16 F10-tagGFP tumors were given an intravenous injection of 100 mg of FTF-TAMRA. The mice were sacrificed 1 h after injection. Tumors were harvested and mechanically dissociated using Micro Tissue Homogenizers (Kimble Biomasher II). Collagenase IV at 0.5 mg/mL in RPMI 1640 was added to the tissues, followed by vigorous shaking at 37 °C for 30 min. The digested tissues were filtered through a 40 μm cell strainer and resuspended in PBS. Cells were stained using Aqua Amine Live Dead Fixable viability stain (Thermo Fisher) and fluorophore-conjugated antibodies (Table S2). The cells/tissues were washed using FACS buffer by centrifugation and were resuspended in 300 μL FACS buffer. The samples were analyzed using an Attune NXT flow cytometer (Thermo Fisher), and data analysis was performed with FlowJo 10 software (TreeStar).

Mouse Models. All animals were obtained from Jackson laboratory (stock no. 000664) and housed under specific pathogen-free conditions at Massachusetts General Hospital. Experiments were approved by the MGH Institutional Animal Care and Use Committee and were performed according to MGH IACUCAC protocol 2013N000157. All mice were provided ad libitum access to food and water and a standard 12 h light/dark cycle. All experiments were performed under isoflurane gas anesthesia. Ten week old male/female C57BL/6J mice were utilized for all experiments. A total of n = 48 were mice used. This included n = 12 mice for flow cytometry, n = 12 mice for ex vivo tumor imaging and n = 24 mice for intravital microscopy.

Tumor Model. For ex vivo B16 F10-GFP tumor imaging, 10^6 B16 F10-GFP tumor cells in 100 μL of serum-free DMEM were injected into the upper rear flanks of mice. Tumors were allowed to grow for 5 days before excision. Excised tumors were rinsed in PBS and then Stained in 500 μM FAPi-FL and 1 μg/mL Hoechst for 10 min in Fluorobrite DMEM (Thermo Fisher), followed by a 10 min wash in Fluorobrite DMEM.

Dorsal Window Chamber Model. Mice bearing DWC with B16 F10-GFP were used to the assess the in vivo uptake kinetics and intratumoral distribution of FTF. DWC were surgically implanted, the upper epidermal layer inside of the DWC was removed and 10^6 B16 F10-GFP tumor cells in 20 μL of Matrigel (Corning) were injected. Tumors were allowed to grow for 8−11 days before imaging was performed. On the day of imaging, mice were injected with 1 μM (100 μL) FTF. To capture kinetics of probe delivery, a confocal stack was acquired every 5 min over the course of 120 min.

Confocal Intravital Imaging. Confocal imaging was performed using a customized Olympus FV1000 confocal microscope (Olympus America). A 2x (XLFluor, NA 0.14), a 4x (UPlanSApo, NA 0.16), and an XLUMPlanFL N 20x (NA 1.0) water immersion objective were used for imaging (Olympus America). Cell nuclei (Hoechst), Tumor cells (B16 F10-TagGFP), and FTF-TAMRA were excited sequentially using a 405 nm, a 473 nm, and a 555 nm diode laser in combination with a DM-405/488/559/635 nm dichroic beam splitter. Emitted light was further separated by beam splitters (SDM-473, SDM-560, and SDM-640) and emission filters BA430-455, BA490-540, BA575-620, and BA655-755 (Olympus America). Confocal laser power was optimized during each imaging session to avoid photobleaching, phototoxicity, or tissue damage.

Image Analysis. All image visualization was performed with Fiji (ImageJ, 2.14.0/1.54F). Images were automatically windowed and leveled to maximize contrast and false-colored to differentiate channels. Image analysis was performed with MATLAB 2023B (Mathworks, Natick, MA).

Co-Localization of FAPi-FL and Anti-FAP Antibody Staining. Both images were filtered with a Gaussian filter with a 3 × 3 kernel to reduce noise. A binary mask of the cells in each image was generated from the anti-FAP image. First, morphological opening was performed using the imopen function and a 4-pixel wide disk structuring element. The output image was then binarized using Otsu's method and the imbinarize function. This mask was applied to each image before generating a binned scatter plot with 250 bins along each axis. A linear fit for each data set was performed and plotted using the built-in polyfit function with a degree of n = 1. A Pearson's correlation coefficient and R^2 value were calculated using the built-in.

Statistics. All statistical data analyses were performed using GraphPad Prism 9 software and results are expressed as mean ± standard deviation. For normally distributed data sets, we used 2-tailed Student's t-test and one-way ANOVA followed by Bonferroni's multiple comparison test. When variables were not normally distributed, we performed nonparametric Mann−Whitney or Kuskal−Wallis tests. p values >0.05 were considered not significant (n.s.), p values <0.05 were considered significant.

■ ASSOCIATED CONTENT

Ⓢ Supporting Information

The Supporting Information is available free of charge at https://pubs.acs.org/doi/10.1021/acs.bioconjchem.4c00426.

    NMR and LCMS spectra, additional experimental and computational characterization (PDF)

■ AUTHOR INFORMATION

Corresponding Author

Ralph Weissleder − *Center for Systems Biology, Massachusetts General Hospital, Boston, Massachusetts 02114, United States; Department of Systems Biology, Harvard Medical School, Boston, Massachusetts 02115, United States;* ⓞ orcid.org/0000-0003-0828-4143; Phone: 617-726-8226; Email: rweissleder@mgh.harvard.edu

Authors

Riley J. Deutsch-Williams − *Center for Systems Biology, Massachusetts General Hospital, Boston, Massachusetts 02114, United States*

Kelton A. Schleyer − *Center for Systems Biology, Massachusetts General Hospital, Boston, Massachusetts 02114, United States;* ⓞ orcid.org/0000-0001-5385-8850

Riddha Das − *Center for Systems Biology, Massachusetts General Hospital, Boston, Massachusetts 02114, United States*

Jasmine E. Carrothers − *Center for Systems Biology, Massachusetts General Hospital, Boston, Massachusetts 02114, United States*

Rainer H. Kohler − *Center for Systems Biology, Massachusetts General Hospital, Boston, Massachusetts 02114, United States;* ⓞ orcid.org/0000-0001-6269-6590

Claudio Vinegoni − *Center for Systems Biology, Massachusetts General Hospital, Boston, Massachusetts 02114, United States*

Complete contact information is available at:
https://pubs.acs.org/10.1021/acs.bioconjchem.4c00426

Author Contributions

Conceptualization: RJDW, RW. Formal analysis: RJDW, KS, RD. Investigation: All coauthors. Synthesis and characterization: RJDW, KS. Software: RJDW. Validation: RHK, CV, RW. Supervision: RW Visualization: RJDW, RD, JC, RW. Writing-original draft: RJDW, RW. Writing-review and editing: all coauthors. Funding acquisition: RW. Project administration: RW. Resources: RW.

Notes

The authors declare the following competing financial interest(s): RW is a consultant to Boston Scientific, Earli, and Accure Health, none of whom contributed to this research. The other authors report no affiliations.

■ REFERENCES

(1) Sahai, E.; Astsaturov, I.; Cukierman, E.; DeNardo, D. G.; Egeblad, M.; Evans, R. M.; Fearon, D.; Greten, F. R.; Hingorani, S. R.; Hunter, T.; et al. A framework for advancing our understanding of cancer-associated fibroblasts. *Nat. Rev. Cancer* **2020**, *20*, 174−186.

(2) Flier, J. S.; Underhill, L. H.; Dvorak, H. F. Tumors: Wounds That Do Not Heal. *N. Engl. J. Med.* **1986**, *315*, 1650−1659.

(3) Powell, D. W.; Adegboyega, P. A.; Di Mari, J. F.; Mifflin, R. C. Epithelial cells and their neighbors I. Role of intestinal myofibroblasts in development, repair, and cancer. *Am. J. Physiol.: Gastrointest. Liver Physiol.* **2005**, *289*, G2−G7.

(4) Arina, A.; Idel, C.; Hyjek, E. M.; Alegre, M.-L.; Wang, Y.; Bindokas, V. P.; Weichselbaum, R. R.; Schreiber, H. Tumor-associated fibroblasts predominantly come from local and not circulating precursors. *Proc. Natl. Acad. Sci. U.S.A.* **2016**, *113*, 7551−7556.

(5) Cords, L.; Tietscher, S.; Anzeneder, T.; Langwieder, C.; Rees, M.; de Souza, N.; Bodenmiller, B. Cancer-associated fibroblast classification in single-cell and spatial proteomics data. *Nat. Commun.* **2023**, *14*, 4294.

(6) Cai, Z.; Chen, L.; Chen, S.; Fang, R.; Chen, X.; Lei, W. Single-cell RNA sequencing reveals pro-invasive cancer-associated fibroblasts in hypopharyngeal squamous cell carcinoma. *Cell Commun. Signaling* **2023**, *21*, 292.

(7) Kalaei, Z.; Manafi-Farid, R.; Rashidi, B.; Kiani, F. K.; Zarei, A.; Fathi, M.; Jadidi-Niaragh, F. The Prognostic and therapeutic value and clinical implications of fibroblast activation protein-α as a novel biomarker in colorectal cancer. *Cell Commun. Signaling* **2023**, *21*, 139.

(8) Bonneau, C.; Eliès, A.; Kieffer, Y.; Bourachot, B.; Ladoire, S.; Pelon, F.; Hequet, D.; Guinebretière, J. M.; Blanchet, C.; Vincent-Salomon, A.; et al. A subset of activated fibroblasts is associated with distant relapse in early luminal breast cancer. *Breast Cancer Res.* **2020**, *22*, 76.

(9) Costa, A.; Kieffer, Y.; Scholer-Dahirel, A.; Pelon, F.; Bourachot, B.; Cardon, M.; Sirven, P.; Magagna, I.; Fuhrmann, L.; Bernard, C.; et al. Fibroblast Heterogeneity and Immunosuppressive Environment in Human Breast Cancer. *Cancer Cell* **2018**, *33*, 463−479.e10.

(10) Hamson, E. J.; Keane, F. M.; Tholen, S.; Schilling, O.; Gorrell, M. D. Understanding fibroblast activation protein (FAP): substrates, activities, expression and targeting for cancer therapy. *Proteomics: Clin. Appl.* **2014**, *8*, 454−463.

(11) Song, H.; Xu, M.; Cai, J.; Chen, J.; Liu, Y.; Su, Q.; Li, Z.; Liu, Z. 225Ac-Labeled Antibody for Fibroblast Activation Protein-Targeted Alpha Therapy. *Chem. Biomed. Imaging* **2023**, *1*, 628−636.

(12) Zana, A.; Puig-Moreno, C.; Bocci, M.; Gilardoni, E.; Di Nitto, C.; Principi, L.; Ravazza, D.; Rotta, G.; Prodi, E.; De Luca, R.; et al. A Comparative Analysis of Fibroblast Activation Protein-Targeted Small Molecule-Drug, Antibody-Drug, and Peptide-Drug Conjugates. *Bioconjugate Chem.* **2023**, *34*, 1205−1211.

(13) Mori, Y.; Dendl, K.; Cardinale, J.; Kratochwil, C.; Giesel, F. L.; Haberkorn, U. FAPI PET: Fibroblast Activation Protein Inhibitor Use in Oncologic and Nononcologic Disease. *Radiology* **2023**, *306*, No. e220749.

(14) Jansen, K.; Heirbaut, L.; Cheng, J. D.; Joossens, J.; Ryabtsova, O.; Cos, P.; Maes, L.; Lambeir, A. M.; De Meester, I.; Augustyns, K.; et al. Selective Inhibitors of Fibroblast Activation Protein (FAP) with a (4-Quinolinoyl)-glycyl-2-cyanopyrrolidine Scaffold. *ACS Med. Chem. Lett.* **2013**, *4*, 491−496.

(15) Lindner, T.; Loktev, A.; Altmann, A.; Giesel, F.; Kratochwil, C.; Debus, J.; Jäger, D.; Mier, W.; Haberkorn, U. Development of

Quinoline-Based Theranostic Ligands for the Targeting of Fibroblast Activation Protein. *J. Nucl. Med.* **2018**, *59*, 1415−1422.

(16) Chandekar, K. R.; Prashanth, A.; Vinjamuri, S.; Kumar, R. FAPI PET/CT Imaging-An Updated Review. *Diagnostics* **2023**, *13*, 2018.

(17) Sollini, M.; Kirienko, M.; Gelardi, F.; Fiz, F.; Gozzi, N.; Chiti, A. State-of-the-art of FAPI-PET imaging: a systematic review and meta-analysis. *Eur. J. Nucl. Med. Mol. Imaging* **2021**, *48*, 4396−4414.

(18) Roy, J.; Hettiarachchi, S. U.; Kaake, M.; Mukkamala, R.; Low, P. S. Design and validation of fibroblast activation protein alpha targeted imaging and therapeutic agents. *Theranostics* **2020**, *10*, 5778−5789.

(19) Zhao, X.; Zhang, G.; Chen, J.; Li, Z.; Shi, Y.; Li, G.; Zhai, C.; Nie, L. A rationally designed nuclei-targeting FAPI 04-based molecular probe with enhanced tumor uptake for PET/CT and fluorescence imaging. *Eur. J. Nucl. Med. Mol. Imaging* **2024**, *51*, 1593−1604.

(20) Millul, J.; Bassi, G.; Mock, J.; Elsayed, A.; Pellegrino, C.; Zana, A.; Dakhel Plaza, S.; Nadal, L.; Gloger, A.; Schmidt, E.; et al. An ultra-high-affinity small organic ligand of fibroblast activation protein for tumor-targeting applications. *Proc. Natl. Acad. Sci. U.S.A.* **2021**, *118*, No. e2101852118.

(21) Loktev, A.; Lindner, T.; Mier, W.; Debus, J.; Altmann, A.; Jäger, D.; Giesel, F.; Kratochwil, C.; Barthe, P.; Roumestand, C.; et al. A Tumor-Imaging Method Targeting Cancer-Associated Fibroblasts. *J. Nucl. Med.* **2018**, *59*, 1423−1429.

(22) Entenberg, D.; Oktay, M. H.; Condeelis, J. S. Intravital imaging to study cancer progression and metastasis. *Nat. Rev. Cancer* **2023**, *23*, 25−42.

(23) Madonna, M. C.; Duer, J. E.; Lee, J. V.; Williams, J.; Avsaroglu, B.; Zhu, C.; Deutsch, R.; Wang, R.; Crouch, B. T.; Hirschey, M. D.; et al. In vivo optical metabolic imaging of long-chain fatty acid uptake in orthotopic models of triple-negative breast cancer. *Cancers* **2021**, *13*, 148.

(24) Alieva, M.; Ritsma, L.; Giedt, R. J.; Weissleder, R.; van Rheenen, J. Imaging windows for long-term intravital imaging: General overview and technical insights. *Intravital* **2014**, *3*, No. e29917.

(25) Korolj, A.; Kohler, R. H.; Scott, E.; Halabi, E. A.; Lucas, K.; Carlson, J. C. T.; Weissleder, R. Perfusion Window Chambers Enable Interventional Analyses of Tumor Microenvironments. *Adv. Sci.* **2023**, *10*, No. e2304886.

(26) Halabi, E. A.; Weissleder, R. Light-Deactivated Fluorescent Probes (FLASH-Off) for Multiplexed Imaging. *J. Am. Chem. Soc.* **2023**, *145*, 8455−8463.

(27) Ko, J.; Lucas, K.; Kohler, R.; Halabi, E. A.; Wilkovitsch, M.; Carlson, J. C. T.; Weissleder, R. In Vivo Click Chemistry Enables Multiplexed Intravital Microscopy. *Adv. Sci.* **2022**, *9*, No. e2200064.

(28) Pucci, F.; Garris, C.; Lai, C. P.; Newton, A.; Pfirschke, C.; Engblom, C.; Alvarez, D.; Sprachman, M.; Evavold, C.; Magnuson, A.; et al. SCS macrophages suppress melanoma by restricting tumor-derived vesicle-B cell interactions. *Science* **2016**, *352*, 242−246.